frontiers in Materials

ORIGINAL RESEARCH
published: 29 October 2020
doi: 10.3389/fmats.2020.537812

Fine-Grained FeCoNi(CuAl)$_x$ High Entropy Alloys: Phase Transformation, Microstructure Evolution and Mechanical Properties

Yan Long[1]*, *Guiqi Li*[2], *Xiaobiao Liang*[2] and *Haiyan Peng*[1]

[1]Guangdong Key Laboratory for Advanced Metallic Materials, School of Mechanical and Automotive Engineering, South China University of Technology, Guangzhou, China, [2]National Near-Net-Shape Forming Engineering Research Center for Metallic Materials, Guangzhou, China

A series of fine-grained FeCoNi(CuAl)$_x$ (x = 0, 0.4, 0.6, 0.8, 1.0) medium-entropy alloy (MEA) and high-entropy alloys (HEAs) were fabricated by Mechanical Alloying (MA) and Spark Plasma Sintering (SPS). The effect of Al and Cu content (x) on phase composition, microstructure, and mechanical properties of the alloys was investigated. Experimental results show that the crystal structure of FeCoNi(CuAl)$_x$ alloy transforms from single (face-centered cubic) FCC phase for x = 0 to FCC + BCC duplex phases for x = 0.4~1.0, with the fraction of (body-centered cubic) BCC phase gradually increasing with the increase of x. Adding a low content of Al and Cu elements to FeCoNi alloy can significantly hinder the grain growth during sintering process, the average grain size of FCC phase decreases from 0.95 to 0.30 μm at x = 0.4. However, the grain sizes of FCC and BCC phases gradually grow up when x increases from 0.4 to 1.0. The variation in grain size indicates that the atomic diffusion rate of sintered alloy may be influenced by the sluggish diffusion effect in HEA as well as the content of Al and Cu with lower melting points. Mechanical properties of the HEAs are mainly affected by the volume fraction of BCC phase. The compressive yield strength and hardness of HEAs are improved at first and then slightly reduced, while the plasticity drops down continuously with the increase of x. The bulky HEA achieved excellent comprehensive mechanical properties with a compressive yield strength of 1,467.7 MPa and plastic strain to failure of 24.9% at x = 0.6, due to the fine duplex microstructure.

Keywords: high-entropy alloys, phase transformation, fine-grained, mechanical properties, spark plasma sintering

OPEN ACCESS

Edited by:
Suryanarayana Challapalli, University of Central Florida, United States

Reviewed by:
Ho Jin Ryu, Korea Advanced Institute of Science and Technology, South Korea
Peter K Liaw, The University of Tennessee, United States

***Correspondence:**
Yan Long
ylong1@scut.edu.cn

Specialty section:
This article was submitted to Mechanics of Materials, a section of the journal Frontiers in Materials

Received: *25 February 2020*
Accepted: *23 September 2020*
Published: *29 October 2020*

Citation:
Long Y, Li G, Liang X and Peng H (2020) Fine-Grained FeCoNi(CuAl)$_x$ High Entropy Alloys: Phase Transformation, Microstructure Evolution and Mechanical Properties. Front. Mater. 7:537812. doi: 10.3389/fmats.2020.537812

INTRODUCTION

Different from traditional alloy design strategies, the concept of high-entropy alloys (HEAs) was first proposed by Yeh et al. in 2004. Generally, HEAs consist of at least five constituents in equimolar or near equimolar proportions, with atomic concentration ranging between 5% and 35% (Yeh et al., 2004; Ye et al., 2016; Miracle and Senkov, 2017). Due to their special multiple-principal-element composition and high configurational entropy, HEAs generally tend to form simple solid solution phases like face-centered cubic (FCC), body-centered cubic (BCC), hexagonal close-packed (HCP) phases or a mixture of them. In addition, some HEAs have promising properties, such as excellent mechanical properties (Zhang et al., 2014; Fu et al., 2018; Lei et al., 2018; Long et al., 2019; Zhang

et al., 2020), oxidation resistance (Nong et al., 2018), high-temperature mechanical properties (Senkov et al., 2018a; Senkov et al., 2018b; Senkov et al., 2018c), outstanding wear resistance (Ye et al., 2018; Li et al., 2019) and corrosion resistance (Fujieda et al., 2017; Luo et al., 2018; Zhou et al., 2019), and so on. This new alloy system has been extensively researched in recent years.

FeCoNiCr-based HEA is one of the earliest proposed and most intensively investigated alloy systems. They usually consist of single-phase FCC structure or FCC + BCC dual-phase structure. Generally, single FCC-phase HEAs are ductile but soft (Li et al., 2017; Xiang et al., 2019), and single BCC-phase HEAs have high strength but are less ductile (Senkov et al., 2011; Zhang et al., 2012), while a combination of these two phases can make a good balance between strength and ductility (Lu et al., 2014). The general strengthening method of FeCoNiCr HEA is adding other elements (Al, Ti, Mn, Cu, Mo, etc.) to study their effects on the phase composition and mechanical properties [such as FeCoNiCrCu (Zhang et al., 2011), FeCoNiCrAl (Tian et al., 2019), FeCoNiCrMn (Han et al., 2019), FeCoNiCrMo$_x$ (Liu et al., 2016), etc.]. Tong et al. (2019) prepared a precipitation-strengthened FeCoNiCrTi$_{0.2}$ high-entropy alloy using arc melting and casting methods. It exhibits a great increase in yield strength ($\sigma_{0.2}$) and ultimate tensile strength (σ_{UTS}), with little loss in ductility at room temperature compared with the single-phase FeCoNiCr parent alloy; in addition, at cryogenic temperatures, its $\sigma_{0.2}$ and σ_{UTS} are increased from 700 MPa to 1.24 GPa to 860 MPa and 1.58 GPa, respectively, associated with a ductility improvement from 36% to 46%. In recent years, systematic studies on FeCoNiCuAl HEA and its variant alloys prepared by different methods have been carried out. Zhuang et al. (2012) and Zhuang et al. (2013) studied the microstructure and mechanical properties of a series of FeCoNiCuAl high-entropy alloys in as-cast and heat-treated conditions. During the casting process of FeCoNiCuAl HEA, Cu element tends to segregate to interdendritic regions, which affects the comprehensive properties of the material. Fu et al. (2016) prepared a CoNiFeAl$_{0.3}$Cu$_{0.7}$ HEA with single-phase FCC structure by a combination method of Mechanical Alloying (MA) and Spark Plasma Sintering (SPS). Its yield strength and hardness were 1795 MPa and 454 Hv, respectively. Compared with the casting method, the combination of MA + SPS has advantages of low-temperature sintering, rapid sintering, multi-field coupling, etc., which makes the prepared alloys have the characteristics of high density, fine grains, uniform microstructure and less segregation.

According to earlier researches (Tung et al., 2007; Li et al., 2010; Yang et al., 2015; Matusiak et al., 2019), in FeCoNiCuAl HEAs, Al element can promote the formation of BCC phase, while Cu element can stabilize FCC phase. Actually, the addition of Al and Cu into FeCoNi medium-entropy alloy (MEA) might not only increase the entropy of alloy, lead to the phase transformation, but also influence the diffusion rate and grain growth of the alloy at elevated temperature. In the present work, the competitive influence of Al and Cu elements on the phase formation of the alloy was researched, bulky FeCoNi(CuAl)$_x$ (x = 0~1, means the content of Cu and Al elements) MEA and HEA samples with fine grains were prepared by powder metallurgy method (MA + SPS), the mechanical alloying behavior of powders during ball milling process and the phase formation of bulky MEA and HEAs during sintering were analyzed; the grain sizes in various sintered samples were measured in order to evaluate the atomic diffusion rate of HEAs; meanwhile, the effects of Al and Cu content on phase formation, microstructure evolution and mechanical properties of FeCoNi(CuAl)$_x$ (x = 0, 0.4, 0.6, 0.8, 1.0) MEA and HEAs were also investigated.

EXPERIMENTAL

In the present experiment, five kinds of elemental powders, Fe, Co, Ni, Cu and Al, with purity greater than 99.9 wt%, were used as raw materials. Their physical properties are shown in **Table 1**. These five elements were mixed with each other in proportions of FeCoNi(CuAl)$_x$ (x = 0, 0.4, 0.6, 0.8, 1.0), the mixing enthalpy among the relative elements are shown in **Table 2**.

The mixed powders were then placed in a stainless-steel ball mill tank at a ball-to-material ratio of 12:1 and the MA process was performed under the protection of high purity argon atmosphere. In the vacuum glove box, a small amount of powders ball-milled for 10, 20, 30 and 40 h were taken out for analysis. The powders ball milled for 40 h were subsequently consolidated in a graphite die by a spark plasma sintering (SPS) machine (Sumitomo Coal Mining Co., Ltd., Japan) at 1,100°C for 10 min in vacuum atmosphere. The sintering pressure was 50 MPa. The powders were heated to the sintering temperature at the heating rate of 100°C min^{-1}. The fabricated bulky HEA samples were cylinders with a diameter of 20 mm and height of 10 mm.

The phase analysis of ball milled powders and sintered samples were conducted by a Bruker D8 ADVANCE X-ray diffractometer (XRD) with a rotating Cu anode and cross-beam optics selection Cu-K$_\alpha$ ($\lambda_{\alpha1}$ = 1.54059 Å, $\lambda_{\alpha2}$ = 1.54441 Å). Its scanning step was 0.02° and the angular 2θ range was 20° < 2θ < 100°. The thermal analysis of the alloy powders milled for 40 h were performed in the Differential Scanning Calorimeter (DSC, NETZSCH STA 449C) from room temperature to 1,280°C with a heating rate of 10 K min^{-1} under flowing high purity argon atmosphere. Microstructures of sintered samples were observed by Scanning Electron Microscope (SEM, Nova Nano SEM 430, United States). The phase composition and microstructure of bulk alloys were analyzed by Transmission Electron Microscope (TEM, TECHNAL G2 F20 S-TWIN, United States) with an EDS. Specimens for TEM tests were thinned by mechanical polishing and then via ion beam thinning. After that, the samples were cleaned with acetone first and then with absolute ethyl alcohol. The electron back-scattered diffraction (EBSD) was used to investigate the phase distribution of sintered samples, mechanically polished and ion polished specimens were used for observation. Densities of consolidated alloy samples were measured by Archimedes principle method. The measuring medium was deionized water. The hardness test (according to the Chinese national standard-GB/T 4340.1-2009) was carried out by a digital Micro Hardness (Tester HVS-1000 Vickers hardness apparatus) at a load of 500 gf holding for 20 s. Ten

TABLE 1 | Characteristic parameters of alloy elements.

Element	Molar mass (g mol^{-1})	Lattice constant (Å)	Atomic radius (Å)	Electronegativity	Melting point (K)	Density (g cm^{-3})	Crystal structure
Fe	55.85	2.87	1.26	1.83	1,811	7.87	BCC
Co	58.93	2.51	1.25	1.88	1,768	8.9	HCP
Ni	58.69	3.52	1.24	1.91	1,728	8.91	FCC
Cu	63.55	3.61	1.28	1.90	1,358	8.96	FCC
Al	26.89	4.05	1.43	1.61	933	2.70	FCC

TABLE 2 | Mixing enthalpy of atomic pairs (kJ mol^{-1}).

Element	Fe	Co	Ni	Cu	Al
Fe	—	–1	–2	13	–11
Co	—	—	0	6	–19
Ni	—	—	—	4	–22
Cu	—	—	—	—	–1
Al	—	—	—	—	—

points were evenly selected on the sample for measurement to obtain the average value, with each indent spaced about 0.5 mm from one another. The samples for XRD, SEM, Density and Hardness test were cut to the size of 6 × 6 × 8 mm, then mechanically polished and ultrasonic cleaned. Compressive properties at room temperature were measured by a universal testing machine (AG-100 KNx, Shimadzu Corporation, Japan) at a strain rate of 10^{-3} s^{-1} using cylinder specimens with the size of Φ3 × 6 mm and three compression specimens were measured for each component. In order to avoid the influence of carbon diffusion during sintering, the surface of sintered samples were cut off by 1 mm by wire electrical discharge machining before sampling and analyzing.

RESULTS AND DISCUSSION

Phase Transformation and Microstructure Evolution

X-ray diffraction (XRD) patterns illustrate the mechanical alloying process of pre-mixed elemental powders with different compositions during ball milling and their phase compositions, as shown in **Figure 1**. It is found that with the increase of milling time, the intensities of diffraction peaks of original elements decrease sharply and meanwhile peaks of a new solid solution phase emerge. After ball milling for 20~40 h, single FCC phases are identified as basic crystal structure in the mechanically alloyed powders. It is noticed that when the content of Al and Cu elements increases from 0 to 1.0, the mechanical alloying rate becomes slower, indicating that the addition of Al and Cu elements to Fe-Co-Ni powders slows down the process of mechanical alloying and increases the time required to form a solid solution phase, without affecting the final solid solution structure. According to **Table 1**, Fe, Co, and Ni have similar electronic structure and atomic radius, so these three elements tend to form substitutional solid solution easily in the process of mechanical alloying. When Cu and Al elements are added, due to their relatively large atomic radius, large lattice distortion would be introduced during the alloying process, and the number of elements also increases, which might hinder the mechanical alloying process. In high-entropy alloys, the formation of a new phase depends on the cooperative diffusion of many different kinds of atoms, the interaction between different kinds of atoms and the severe lattice distortion would decrease the effective diffusion rate in HEAs and thus the mechanical alloying time needed to form a solid solution phase would increase. Furthermore, the grain size and lattice strain of the respective powders ball milled for 40 h are calculated from the diffraction peak widths by Williamson-Hall equation (Williamson and Hall, 1953) and are given in **Table 3**. After ball milling for 40 h, the average grain sizes of powders are reduced to 12.71~29.83 nm.

DSC curves for FeCoNi(CuAl)$_x$ alloy powders milled for 40 h are shown in **Figure 2**. There are no obvious exothermic or endothermic peaks in the DSC curve for x = 0, which means during the heating process the powder has good thermal stability and remains the single FCC structure. In the range of $0.4 \leq x \leq 0.8$, the DSC curves exhibit obvious endothermic and exothermic peaks, indicating the occurrence of phase transformation, i.e., precipitation and solid dissolution of second phase during the heating process. As x reaches 1.0, it can be seen that the DSC curve has a clear exothermic peak at 313.7°C, while the endothermic peak is hardly visible. Comparing the exothermic peaks of various FeCoNi(CuAl)$_x$ alloy powders in **Figure 2**, it is found that with the increase of Al and Cu content, the FCC solid solution generated by mechanical alloying becomes more unstable and the precipitation temperature of the second phase is descending.

Figure 3 shows XRD results of bulky MEA and HEA sintered samples. It is revealed that the sintered samples remain the single FCC crystal structure in the FeCoNi MEA; but while the content of Cu and Al increases, BCC phase is generated from the FCC matrix during the sintering process and the sintered HEAs exhibit BCC + FCC dual-phase structures. The XRD results of the sintered samples confirm the phase transformation shown in **Figure 2**. The exothermic peaks observed in **Figure 2** correspond to the precipitation of BCC phase from the supersaturated FCC alloy powders at a lower temperature and the endothermic peaks in it indicate partial solid solution of BCC phase into FCC matrix at a higher temperature.

According to the diffraction peak strength of FCC and BCC phases shown in **Figure 3**, it is clearly seen that the fraction of BCC phase increases obviously with the increase of Al and Cu contents. It is suggested that the increase of Al and Cu contents will promote the formation of BCC phase in FeCoNi(CuAl)$_x$ alloys, and make its structure change from single FCC phase to

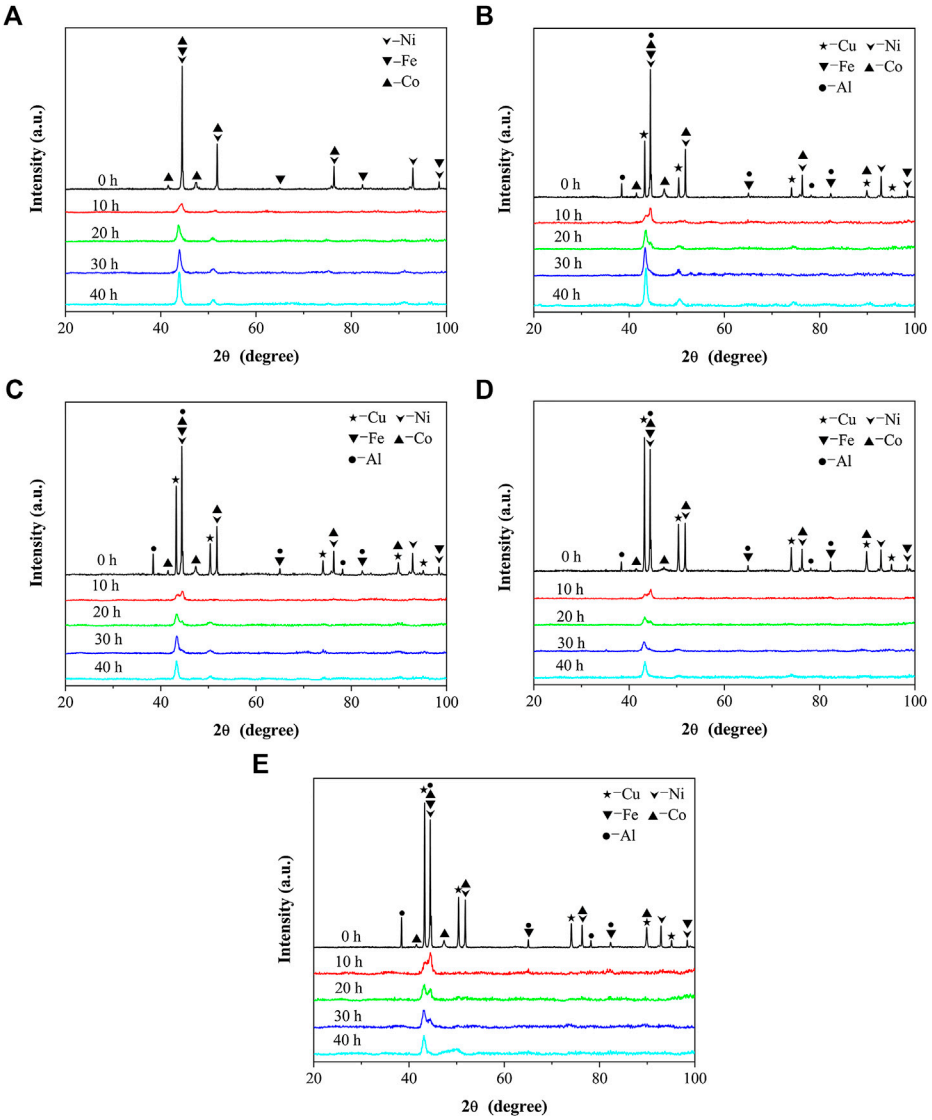

FIGURE 1 | XRD patterns of FeCoNi(CuAl)$_x$ MEA and HEA powders with different milling times: **(A)** x = 0; **(B)** x = 0.4; **(C)** x = 0.6; **(D)** x = 0.8; **(E)** x = 1.0.

TABLE 3 | Average grain sizes, lattice strains and lattice constants of 40 h-milled FeCoNi(CuAl)$_x$ MEA and HEA powders.

Alloy	Grain size (nm)	Lattice strain ε (%)	Lattice constant (nm)
x = 0	29.83	0.95	0.35725
x = 0.4	12.71	0.95	0.36009
x = 0.6	18.47	0.91	0.36196
x = 0.8	20.89	1.08	0.36177
x = 1.0	14.60	1.56	0.36311

FCC + BCC dual-phase. Additionally, we can see from **Table 4**, the lattice constants of FCC and BCC phases are continuously increased with the increase of x due to the addition of Al and Cu with relatively large atomic radius. As previously reported, Al promotes the formation of BCC phase, while Cu lead to the formation of FCC phase (Tung et al., 2007; Li et al., 2010; Yang et al., 2015; Matusiak et al., 2019). When the content of Al and Cu changes at the same time in the present work, the effect is similar with that of changing the Al content alone, which demonstrates that in the competition between the two elements Al dominates the phase formation in the HEA.

The microstructure of FeCoNi(CuAl)$_x$ bulk alloys sintered at 1,100°C was observed and analyzed by Scanning Electron Microscope (SEM). The back scattering images are presented in **Figure 4**. Single FCC phase matrix and a small amount of oxides are observed at x = 0, the volume fraction of oxides is about 4.4%; and the HEA basically remains single phase structure for x = 0.4. In the specimens with x ranging from 0.6 to 1.0, it can be seen clearly that there are two kinds of phases in the microstructure, that is, light gray phase and dark phase, which are consistent with XRD results. While x = 0.6, the second phase

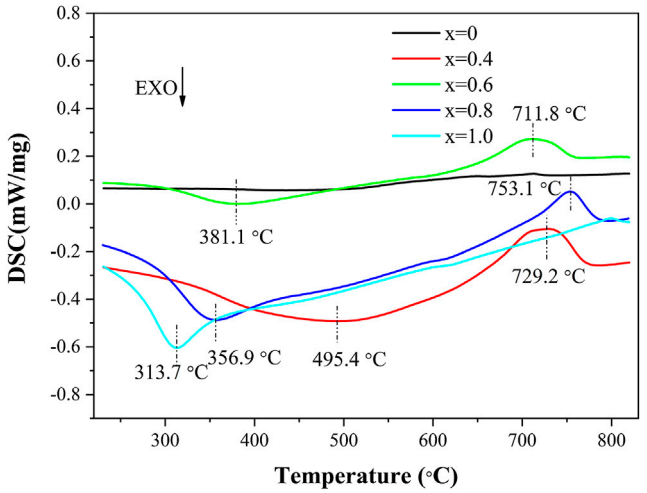

FIGURE 2 | DSC curves of 40 h-milled FeCoNi(CuAl)$_x$ MEA and HEA powders.

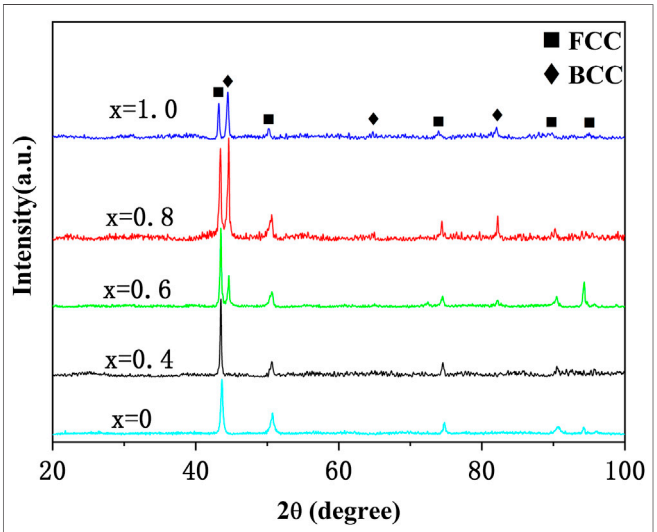

FIGURE 3 | XRD patterns of sintered bulky FeCoNi(CuAl)$_x$ MEA and HEAs.

TABLE 4 | Lattice parameters, lattice strain and phase fraction of FeCoNi(CuAl)x MEA and HEAs.

Alloy	Lattice constant (nm)		Lattice strain ε (%)	
	FCC	BCC	FCC	BCC
x = 0	0.35922	—	0.38	—
x = 0.4	0.36014	—	0.17	—
x = 0.6	0.36055	0.28718	0.32	0.27
x = 0.8	0.36076	0.28774	0.28	0.34
x = 1.0	0.36251	0.28803	0.26	0.33

disperses uniformly on the matrix in a granular morphology. With the continuous increase of the contents of Al and Cu elements, the second phase increases significantly and its distribution tends to be agglomerated and entangled gradually. It is also found from **Figure 4** that the FeCoNi (x = 0) ternary alloy contains more oxides than other alloys that containing Al and Cu elements. It is previously reported that adding Al element to FeCoNi alloy can effectively limit the formation of oxides (Butler and Weaver, 2016).

Figure 5 illustrates TEM bright-field image and selected area electron diffraction patterns (SAED) of FeCoNi(CuAl)$_x$ (x = 0, 0.4, 0.6, 0.8, 1.0) alloys. Apparently, the sintered alloys exhibit fine equiaxed microstructures. The SAED pattern in **Figure 5A** shows that the FeCoNi ternary alloy consists of single FCC phase and there are a few fine oxide particles at the grain boundary (as pointed by the arrow in **Figure 5A**). The FeCoNi alloy has a wide grain size distribution; the larger grain sizes are above 1 μm while the smaller grain sizes are less than 200 nm. After adding Cu and Al (x = 0.4), the grain sizes of sintered samples become more homogeneous, and the average grain size of FeCoNi(CuAl)$_{0.4}$ high-entropy alloy is significantly reduced, as shown in **Figure 5B**. With the following increase of Al and Cu content, the grain size of the material shows an obvious increasing trend, as seen in **Figures 5C–E**. At x = 1.0, the average grain size of FeCoNiCuAl high-entropy alloy grow up to be close to that of the FeCoNi ternary alloy. For x = 0.4, 0.6, 0.8, 1.0, oxide particles are hardly found in TEM bright-field images, suggesting that the oxidation of HEAs are suppressed by the addtion of Al. SAED analysis of FeCoNi(CuAl)$_x$ (x = 0.4, 0.6, 0.8, 1.0) HEAs shows that FCC and BCC phases both exist in bulky high-entropy alloys with the addition of Al and Cu elements. The insets in **Figure 5D** present the SAED patterns of the selected grains marked as A and B in **Figure 5D**. According to the SAED results, A is indexed to be a FCC structure, while B possesses a BCC structure. The EDS/TEM compositions of each phase for FeCoNi(CuAl)$_x$ (x = 0, 0.4, 0.6, 0.8, 1.0) MEA and HEAs are shown in **Table 5**. The BCC phase is found to be enriched in Al and Ni elements, while FCC phase is enriched in Fe, Co and Cu elements. It should be pointed out that though the existence of BCC phase is not found in the XRD result because of its low volume fraction in the FeCoNi(CuAl)$_{0.4}$ specimen, SAED patterns discovers that miner BCC has been formed in the HEA with x of 0.4.

As the content of Al and Cu increases, the percentage of BCC phase increases. It can be seen from **Table 5** that with the precipitation of BCC phase, Al and Ni are depleted in FCC phase and other elements are enriched in FCC phase, thus makes FCC phase became different from the nominal composition.

According to the theory of solid solution formation (Zhang et al., 2008; Wang et al., 2015), simple solid solution phases are supposed to form when thermodynamic parameters Ω (Zhang et al., 2008), atomic size difference δ (Zhang et al., 2008), and atomic size parameter γ (Wang et al., 2015) of the high-entropy alloys satisfy the conditions that $\Omega \geq 1.1$, $\delta \leq 6.6\%$, and $\gamma \leq 1.175$. It can be seen from **Table 6** that the sintered alloys with various compositions all satisfy this criteria. As to determination of lattice structure, Guo and Liu (2011) and Guo et al. (2011) proposed that single FCC solid solution phase will be formed if VEC > 8. As the VEC of the five high-sintered alloys are greater than 8, these five MEA and HEAs can form single FCC solid solution phase, but actually the sintered alloys prefer to form FCC + BCC two-phase

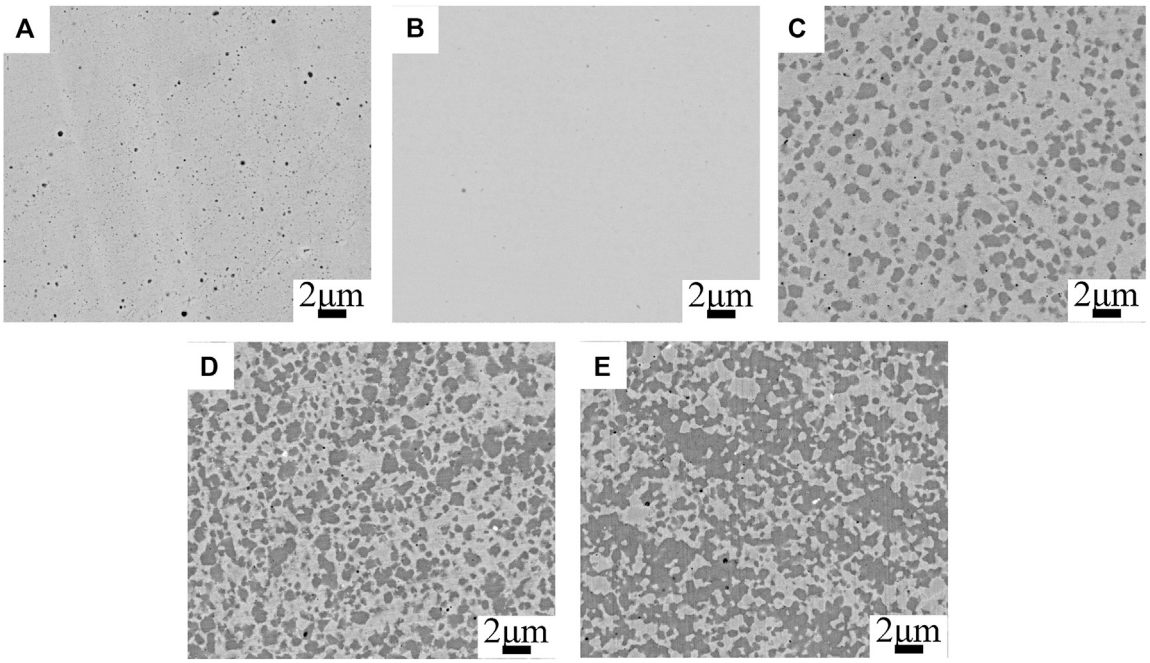

FIGURE 4 | SEM back scatter electron images of the bulk FeCoNi(CuAl)$_x$ MEA and HEAs: **(A)** x = 0; **(B)** x = 0.4; **(C)** x = 0.6; **(D)** x = 0.8; **(E)** x = 1.0.

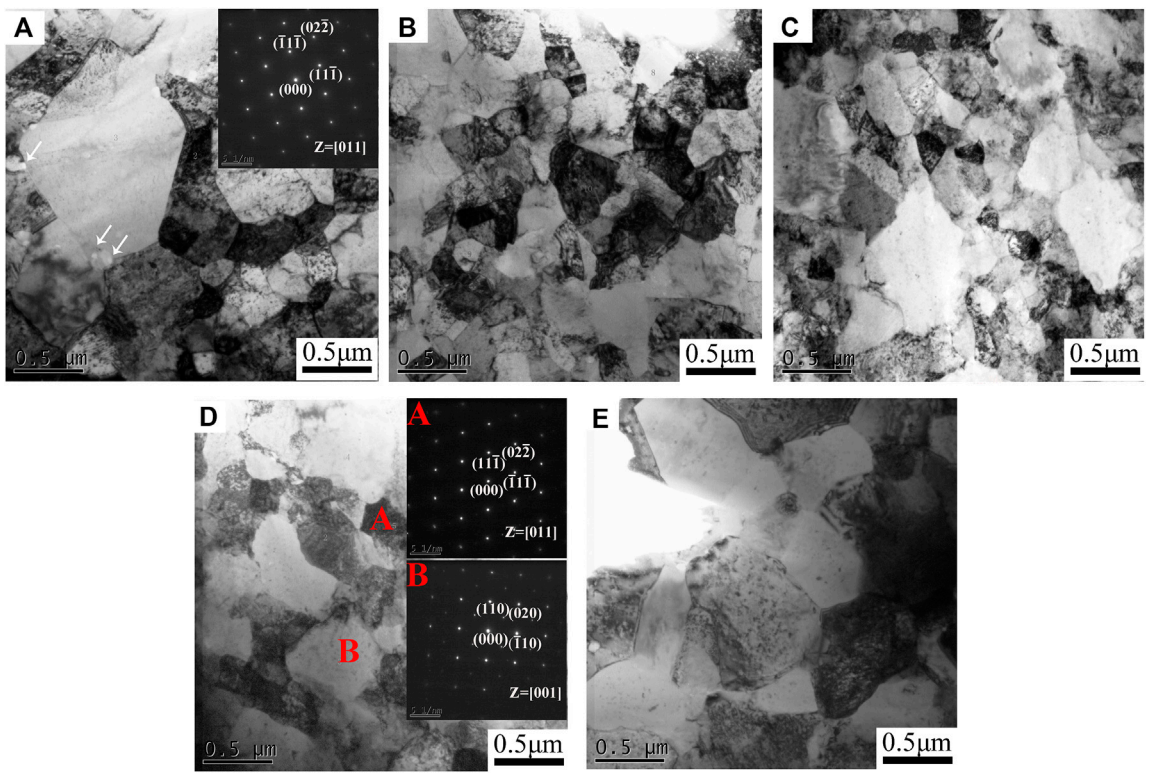

FIGURE 5 | TEM images of bright field and corresponding SAED patterns of bulk FeCoNi(CuAl)$_x$ alloys (x = 0,0.4, 0.6,0.8, 1.0): **(A)** x = 0, inset: SAED pattern of FCC matrix along [011] axis; **(B)** x = 0.4; **(C)** x = 0.6; **(D)** x = 0.8, inset A: SAED pattern of grain A corresponding to a FCC structure along [011] axis; inset B: SAED pattern of grain B corresponding to a BCC structure along [001] axis; (e) x = 1.0.

TABLE 5 | EDS/TEM results (in at%) of the phases of bulk FeCoNi(CuAl)$_x$ MEA and HEAs.

Alloy	Region	Al	Fe	Co	Ni	Cu
x = 0	Nominal composition	—	33.33	33.33	33.33	—
	FCC	—	34.19	32.51	32.30	—
	BCC	—	—	—	—	—
x = 0.4	Nominal composition	10.52	26.32	26.32	26.32	10.52
	FCC	5.60	30.59	27.31	24.52	11.98
	BCC	21.27	21.48	21.22	30.59	5.44
x = 0.6	Nominal composition	14.29	23.81	23.81	23.81	14.29
	FCC	6.67	27.82	27.11	23.16	15.24
	BCC	21.66	22.25	22.07	28.58	5.44
x = 0.8	Nominal composition	17.39	21.74	21.74	21.74	21.74
	FCC	9.68	25.89	22.59	18.78	23.06
	BCC	26.05	18.97	20.40	24.62	9.96
x = 1.0	Nominal composition	20	20	20	20	20
	FCC	11.74	26.94	16.71	17.38	27.23
	BCC	28.37	19.83	17.48	25.07	9.25

alloy except the ternary alloy. It is indicated that the phase formation is not only associated with the composition, but also influenced by the processing temperature. From the former DSC results, phase transformation is observed in the quinary HEAs. During the heating process of mechanically alloyed HEA powders, BCC phase is first precipitated from the supersaturated FCC matrix, and then partially dissolved into the FCC phase with the rising temperature. This result is basically consistent with the FeCoNiCuAl HEA phase diagram previously

TABLE 6 | Relevant parameters of FeCoNi(CuAl)$_x$ MEA and HEAs.

Alloy	ΔS_{mix} (J K^{-1} mol^{-1})	δ (%)	Ω	T_m (K)	ΔH_{mix} (kJ mol^{-1})	VEC	γ
x = 0	9.13	0.65	12.11	1,729	−1.33	9	1.017
x = 0.4	12.70	4.36	5.09	1637.76	−4.09	8.58	1.169
x = 0.6	13.14	4.88	4.44	1590.89	−4.71	8.43	1.169
x = 0.8	13.32	5.21	4.07	1552.17	−5.07	8.30	1.169
x = 1.0	13.37	5.44	3.85	1519.65	−5.28	8.2	1.168

estimated by Beyramali Kivy et al. (2017) that illustrated the phase fraction changes as a function of temperature. At a temperature higher than about 950 K, FeCoNiCuAl HEA tends to exhibit a single FCC phase structure, while at a temperature below ~950 K, FCC solid solution became unstable and there exists a two-phase zone of FCC + BCC phases.

According to Gibbs free energy formula, stability of single-phase solid solution relies on mixing enthalpy and configuration entropy of an alloy system. When configuration entropy dominates in the alloy system, stable single-phase solid solution can be formed. However, in most cases, the enthalpy of mixing and other factors will affect the stability of phases in alloys to a certain extent, leading to formation of multiphase or intermetallic compounds in alloys. If the tendency of forming compounds among alloying elements is relatively large, this tendency will be reflected in the high-entropy alloy. Based on the parameter from **Table 2**, there is a relatively large negative

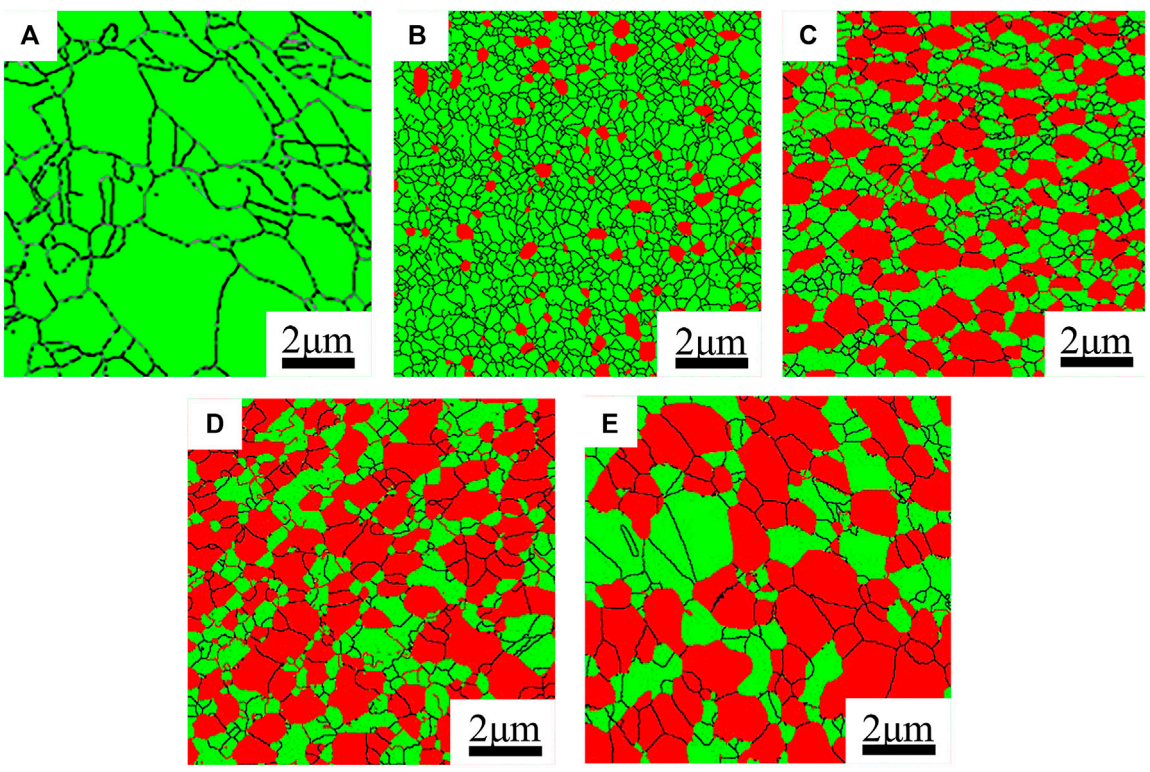

FIGURE 6 | EBSD phase maps of bulk FeCoNi(CuAl)$_x$ MEA and HEAs: **(A)** x = 0; **(B)** x = 0.4; **(C)** x = 0.6; **(D)** x = 0.8; **(E)** x = 1.0 (green-FCC, red-BCC).

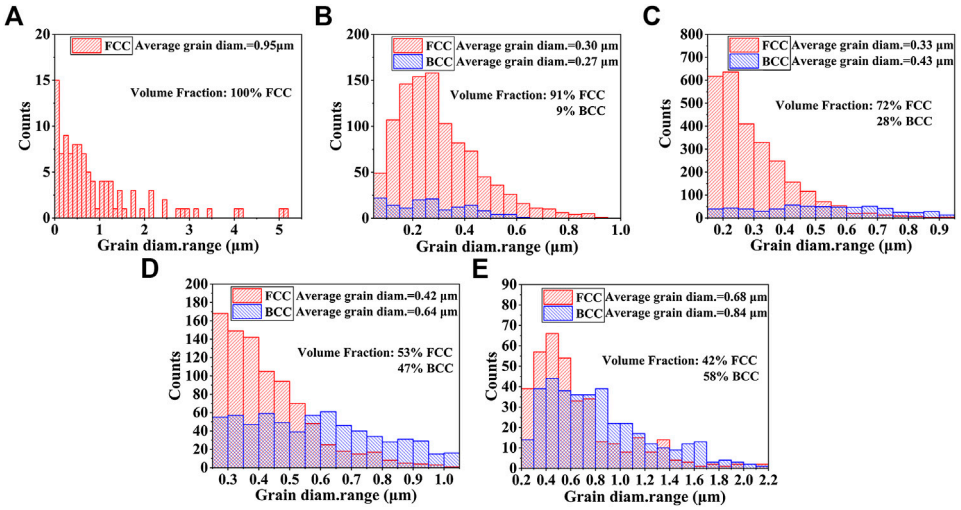

FIGURE 7 | Statistical grain diameter distribution and phase volume fraction of bulk FeCoNi(CuAl)$_x$ MEA and HEAs: **(A)** x = 0; **(B)** x = 0.4; **(C)** x = 0.6; **(D)** x = 0.8; **(E)** x = 1.0.

mixing enthalpy between Al and Ni elements. It can be predicted that in the high-entropy alloy, If the content of Al and Cu elements increases, the second phase rich in Al and Ni elements would inevitably be formed, which can explain the appearance of the second phase in FeCoNi(CuAl)$_x$ HEA samples. In addition, Al atom has the largest atomic radius of 1.43 Å in FeCoNi(CuAl)$_x$ HEAs system. In the process of SPS sintering, Al element tends to precipitate from the FCC matrix by combining with other elements, thus reducing the lattice distortion and elastic energy of the matrix. In fact, this transformation of alloy structure from single FCC phase to FCC + BCC dual-phase caused by changing Al and Cu elements at the same time is similar with the situation of changing Al elements in FeCoNiCuAl (Beyramali Kivy et al., 2017). It is suggested that though Al and Cu contents are changed simultaneously in FeCoNi(CuAl)$_x$ high-entropy alloys, Al element may play a dominant role in the phase transformation. In the process of sintering, the internal stress in the high-energy ball-milled powders is released, the lattice defects are greatly reduced, phase transformation occurs in the supersaturated solid solution by atomic inter-diffusion. Moreover, the ball-milled powders exhibit a severely-plastic-deformed nanocrystalline structure, and a large amount of lattice defects and grain boundaries can promote the diffusion of atoms, thus facilitating the occurrence of phase transformation.

In order to determine the grain size and distribution of each phase, EBSD examination were carried out on FeCoNi(CuAl)$_x$ MEA and HEAs. EBSD results are shown in **Figure 6** and corresponding grain distribution statistical charts and phase volume fraction are illustrated in **Figure 7**. For x = 0, only a single FCC phase structure is observed, and there are a certain number of twin boundaries in the grains. Its average grain size is measured to be 0.95 μm. For x = 0.4, there are a few BCC phase dispersed in the matrix with FCC structure, and the average grain sizes for FCC and BCC phase are dramatically reduced to only

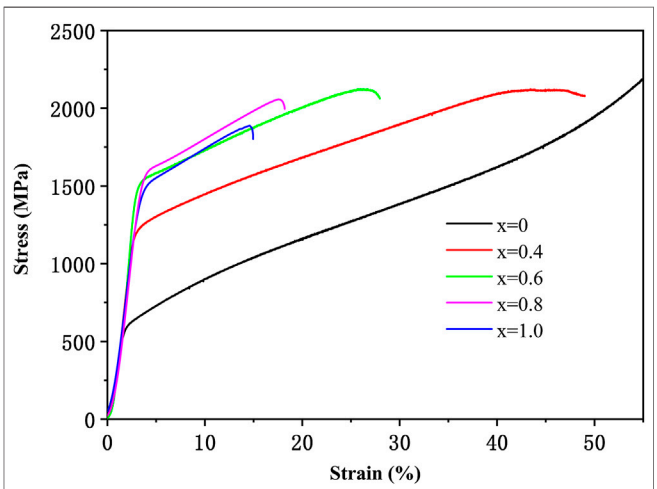

FIGURE 8 | Compressive engineering stress-strain curves of the bulk FeCoNi(CuAl)$_x$ MEA and HEAs.

0.30 and 0.27 μm, respectively. When x increases from 0.4 to 1, the volume fraction of second phase increases continuously, and the second phase begins to agglomerate and form connected regions. At x value of 1.0, its volume fraction arrives at 58%, even exceeding the proportion of FCC phase. Additionally, the grain sizes of two phases grow up with the addition of Al and Cu content. As x increased up to 1.0, the average grain sizes of FCC and BCC phases rise to 0.68 and 0.84 μm, respectively.

While the content of Al and Cu (x) is 0.4, an interesting phenomenon could be seen that the grains of the HEA are refined remarkably in comparison to the ternary alloy (as shown in **Figures 6A,B**). This grain refinement is probably caused by the sluggish diffusion effect due to the addition of Al and Cu, which is previously proposed by Yeh and TONG et al. to explain the

TABLE 7 | Mechanical properties of sintered FeCoNi(CuAl)$_x$ alloys and casting FeCoNi(CuAl)$_{0.8}$ HEA.

Process	Alloy	$\sigma_{0.2}$ (MPa)	σ_{max} (MPa)	ε_p (%)	Hardness (Hv)	Relative density (%)	Reference
MA + SPS	x = 0	574.9	—	—	234.9	96.5	
	x = 0.4	1165.1	2122.5	45.2	356.9	95.4	This work
	x = 0.6	1467.7	2123.2	24.9	412.8	98.4	
	x = 0.8	1470.4	2058.0	14.7	501.1	99.4	
	x = 1.0	1381.2	1887.8	12.4	462.6	96.6	
Cast	x = 0.8	601	1935	37.2	280	—	Li et al., 2018

nano-grained microstructure in HEAs (TONG et al., 2005; Yeh, 2013). Diffusion of elements might be hindered in multi-principle-component alloys because of the large fluctuation of lattice potential energy (LPE) between lattice sites. There may exist plenty of low LPE sites that act as traps for atomic diffusion, and also some high LPE sites that are hard for atoms to jump into, thus leading to the sluggish diffusion effect. The reduced diffusion rate would retard the grain boundary migration and slows down the grain growth during the sintering process. However, with the increase of the content of Al and Cu (x), the grain size increases gradually, and the FeCoNiCuAl specimen with equiatomic ratio has an average grain size almost close to the ternary FeCoNi alloy. This result suggests that the atomic diffusion rate of FeCoNiCuAl HEA can also be affectted by the concentration of Al and Cu elements. When x increase in FeCoNiCuAl HEA, content of Al and Cu elements which have lower melting points keep increasing, thus the activation energy of atomic diffusion is reduced and the diffusion rate in HEAs may be developed, subsequently the grain growth rate is increased in the sintered alloy. Meanwhile, the measured average grain sizes of BCC phases is a bit larger than those of FCC phases due to the higher content of Al in BCC phase and the difference in crystal structure. Anyway, statistical analysis results in **Figure 7** show that all the average grain sizes of the quinary HEA samples are still smaller than the ternary MEA sample, suggesting a reduced atomic diffusion rate in HEAs, if the difference in original grain sizes in the ball milled powders could be ignored.

Mechanical Properties

Figure 8 depicts the compressive engineering stress-strain curves of the as-sintered FeCoNi(CuAl)$_x$ (x = 0, 0.4, 0.6, 0.8, 1.0) MEA and HEA specimens at room temperature. The densities and mechanical properties of FeCoNi(CuAl)$_x$ alloys fabricated by SPS and conventional casting FeCoNi(CuAl)$_{0.8}$ HEA (Li et al., 2018) are summarized in **Table 7**. After SPS, all the alloy samples are sintered to near-full densities (95.4~99.4%). For the FeCoNi MEA specimen, its yield strength is only 574.9 MPa. While the content of Al and Cu is 0.4, a small amount of BCC phase is formed in the matrix, and the grain sizes of the matrix are significantly refined, which doubles the yield strength (from 574.9 to 1,165.1 MPa) and meanwhile remains a good plasticity. When x increases from 0.4 to 0.8, the yield strength ($\sigma_{0.2}$) for as-sintered HEA increases continuously and reaches the maximum value of 1,470.4 MPa, but the plastic strain to fracture (ε_p) exhibits a descending trend. According to previous studies, FCC-structured HEAs always show high plasticity and low strength, while BCC-structured HEAs tend to exhibit relatively high strength and poor plasticity. Thus the increase of the yield strength and decrease of the plasticity can be attributed to the increased volume fraction of BCC phase in the HEAs specimens due to the increase of x. Compared with the as-cast counterpart with the same composition, the sintered FeCoNi(CuAl)$_{0.8}$ HEA specimen exhibits a notable increases of 145% on the yield strength, as a result of the much finer grain size in the sintered alloy. At x = 1.0, though the fraction of BCC phase is increased, the yield strength of the FeCoNiCuAl high-entropy alloy slightly declined. This decrease in strength can be explained by the grain growth in the HEA specimen and the aggregation of the second phase, as seen in **Figure 6**.

As the phase composition of FeCoNi(CuAl)$_x$ alloys varies with the content of Cu and Al, the mechanical properties of this alloy can thus be tailored by designing the microstructure through changing x value. It is seen in **Table 7** that at an x value of 0.6 a combination of relatively high strength and good plasticity is achieved in the sintered HEA. The FeCoNi(CuAl)$_{0.6}$ specimen shows a yield strength of 1,467.7 MPa, plastic strain to failure of 24.9% and hardness of 412 Hv.

CONCLUSIONS

In the present work, fine-grained and high-strength FeCoNi(CuAl)$_x$ (x = 0, 0.4, 0.6, 0.8, 1.0) MEA and HEAs were successfully fabricated by MA and SPS, the microstructure, phase formation and mechanical properties of FeCoNi(CuAl)$_x$ have been systematically investigated.

1) Quinary FeCoNi(CuAl)$_x$ alloys have slower mechanical alloying speeds than the ternary FeCoNi alloy, and the ball milling time for FeCoNi(CuAl)$_x$ alloys to accomplish the mechanical alloying process increases with the increase of x. Supersaturated solid solution with single FCC structure is formed in the mechanically alloyed powders with various compositions after ball milling for 20~40 h. After SPS, the sintered alloys exhibit different microstructures depending on the contents of Cu and Al (x). The FeCoNi MEA without addition of Cu and Al remains the single FCC phase structure, while the HEAs with x range from 0.4 to 1.0 transform into FCC + BCC dual-phase structure, with the BCC phase rich in Al and Ni elements while the FCC phase rich in Fe, Co and Cu elements.
2) EBSD observation results show that the average grain size of sintered samples is significantly reduced with a minor addition of Al and Cu into FeCoNi alloy (x = 0.4). When

the Al and Cu content (x) in FeCoNi(CuAl)$_x$ increases from 0.4 to 1.0, the volume fraction of BCC phase increases, the average grain sizes of FCC and BCC phases grow up continuously and the distribution of two phases turns to be more aggregated. It is suggested that the atomic diffusion and grain growth in FeCoNi(CuAl)$_x$ HEAs during the sintering process are affected by the sluggish diffusion effect as well as the change in melting point of the alloy.

3) When x increases from 0 to 0.8, the compressive yield strength and hardness for FeCoNi(CuAl)$_x$ increase dramatically while the plasticity of the materials decreases gradually, owing to the increased volume fraction of BCC phase. The FeCoNi(CuAl)$_{0.6}$ HEA shows a balanced mechanical properties, with its yield strength and plastic strain to failure arriving at 1,467.4 MPa and 24.9%, respectively.

DATA AVAILABILITY STATEMENT

All datasets generated for this study are included in the article.

AUTHOR CONTRIBUTIONS

YL conceived and designed the experiments. GL, XL, and HP performed the experiments. YL, GL, XL, and HP analyzed the data. YL and GL wrote the paper.

FUNDING

This work was supported by the National Natural Science Foundation of China with grant No. 51104066.

REFERENCES

Beyramali Kivy, M., Asle Zaeem, M., and Lekakh, S. (2017). Investigating phase formations in cast AlFeCoNiCu high entropy alloys by combination of computational modeling and experiments. *Mater. Des.* 127, 224–232. doi:10.1016/j.matdes.2017.04.086

Butler, T. M., and Weaver, M. L. (2016). Oxidation behavior of arc melted AlCoCrFeNi multi-component high-entropy alloys. *J. Alloys Compd.* 674, 229–244. doi:10.1016/j.jallcom.2016.02.257

Fu, Z., Chen, W., Wen, H., Zhang, D., Chen, Z., Zheng, B., et al. (2016). Microstructure and strengthening mechanisms in an FCC structured single-phase nanocrystalline Co25Ni25Fe25Al7.5Cu17.5 high-entropy alloy. *Acta Mater.* 107, 59–71. doi:10.1016/j.actamat.2016.01.050

Fu, Z., Jiang, L., Wardini, J. L., Macdonald, B. E., Wen, H., Xiong, W., et al. (2018). A high-entropy alloy with hierarchical nanoprecipitates and ultrahigh strength. *Sci. Adv.* 4, eaat8712. doi:10.1126/sciadv.aat8712

Fujieda, T., Shiratori, H., Kuwabara, K., Hirota, M., Kato, T., Yamanaka, K., et al. (2017). CoCrFeNiTi-based high-entropy alloy with superior tensile strength and corrosion resistance achieved by a combination of additive manufacturing using selective electron beam melting and solution treatment. *Mater. Lett.* 189, 148–151. doi:10.1016/j.matlet.2016.11.026

Guo, S., and Liu, C. T. (2011). Phase stability in high entropy alloys: Formation of solid-solution phase or amorphous phase. *Prog. Nat. Sci.: Materials International.* 21, 433–446. doi:10.1016/s1002-0071(12)60080-x

Guo, S., Ng, C., Lu, J., and Liu, C. T. (2011). Effect of valence electron concentration on stability of fcc or bcc phase in high entropy alloys. *J. Appl. Phys.* 109, 103505. doi:10.1063/1.3587228

Han, Z., Ren, W., Yang, J., Du, Y., Wei, R., Zhang, C., et al. (2019). The deformation behavior and strain rate sensitivity of ultra-fine grained CoNiFeCrMn high-entropy alloys at temperatures ranging from 77 K to 573 K. *J. Alloys Compd.* 791, 962–970. doi:10.1016/j.jallcom.2019.03.373

Lei, Z., Liu, X., Wu, Y., Wang, H., Jiang, S., Wang, S., et al. (2018). Enhanced strength and ductility in a high-entropy alloy via ordered oxygen complexes. *Nature* 563, 546–550. doi:10.1038/s41586-018-0685-y

Li, C., Li, J. C., Zhao, M., and Jiang, Q. (2010). Effect of aluminum contents on microstructure and properties of AlxCoCrFeNi alloys. *J. Alloys Compd.* 504, S515–S518. doi:10.1016/j.jallcom.2010.03.111

Li, X., Feng, Y., Liu, B., Yi, D., Yang, X., Zhang, W., et al. (2019). Influence of NbC particles on microstructure and mechanical properties of AlCoCrFeNi high-entropy alloy coatings prepared by laser cladding. *J. Alloys Compd.* 788, 485–494. doi:10.1016/j.jallcom.2019.02.223

Li, Z., Tasan, C. C., Pradeep, K. G., and Raabe, D. (2017). A TRIP-assisted dual-phase high-entropy alloy: Grain size and phase fraction effects on deformation behavior. *Acta Mater.* 131, 323–335. doi:10.1016/j.actamat.2017.03.069

Li, Z., Xu, H., Gu, Y., Pan, M., Yu, L., Tan, X., et al. (2018). Correlation between the magnetic properties and phase constitution of FeCoNi(CuAl)$_{0.8}$Ga$_x$ ($0 \leq x \leq 0.08$) high-entropy alloys. *J. Alloys Compd.* 746, 285–291. doi:10.1016/j.jallcom.2018.02.189

Liu, W. H., Lu, Z. P., He, J. Y., Luan, J. H., Wang, Z. J., Liu, B., et al. (2016). Ductile CoCrFeNiMo$_x$ high entropy alloys strengthened by hard intermetallic phases. *Acta Mater.* 116, 332–342. doi:10.1016/j.actamat.2016.06.063

Long, Y., Liang, X., Su, K., Peng, H., and Li, X. (2019). A fine-grained NbMoTaWVCr refractory high-entropy alloy with ultra-high strength: Microstructural evolution and mechanical properties. *J. Alloys Compd.* 780, 607–617. doi:10.1016/j.jallcom.2018.11.318

Lu, Y., Dong, Y., Guo, S., Jiang, L., Kang, H., Wang, T., et al. (2014). A promising new class of high-temperature alloys: eutectic high-entropy alloys. *Sci. Rep.* 4, 6200. doi:10.1038/srep06200

Luo, H., Li, Z., Mingers, A. M., and Raabe, D. (2018). Corrosion behavior of an equiatomic CoCrFeMnNi high-entropy alloy compared with 304 stainless steel in sulfuric acid solution. *Corrosion Sci.* 134, 131–139. doi:10.1016/j.corsci.2018.02.031

Matusiak, K., Berent, K., Marciszko, M., and Cieslak, J. (2019). The experimental and theoretical study on influence of Al and Cu contents on phase abundance changes in Al$_x$Cu$_y$FeCrNiCo HEA system. *J. Alloys Compd.* 790, 837–846. doi:10.1016/j.jallcom.2019.03.162

Miracle, D. B., and Senkov, O. N. (2017). A critical review of high entropy alloys and related concepts. *Acta Mater.* 122, 448–511. doi:10.1016/j.actamat.2016.08.081

Nong, Z.-S., Lei, Y.-N., and Zhu, J.-C. (2018). Wear and oxidation resistances of AlCrFeNiTi-based high entropy alloys. *Intermetallics* 101, 144–151. doi:10.1016/j.intermet.2018.07.017

Senkov, O. N., Jensen, J. K., Pilchak, A. L., Miracle, D. B., and Fraser, H. L. (2018a). Compositional variation effects on the microstructure and properties of a refractory high-entropy superalloy AlMo$_{0.5}$NbTa$_{0.5}$TiZr. *Mater. Des.* 139, 498–511. doi:10.1016/j.matdes.2017.11.033

Senkov, O. N., Miracle, D. B., Chaput, K. J., and Couzinie, J.-P. (2018b). Development and exploration of refractory high entropy alloys-A review. *J. Mater. Res.* 33, 3092–3128. doi:10.1557/jmr.2018.153

Senkov, O. N., Rao, S., Chaput, K. J., and Woodward, C. (2018c). Compositional effect on microstructure and properties of NbTiZr-based complex concentrated alloys. *Acta Mater.* 151, 201–215. doi:10.1016/j.actamat.2018.03.065

Senkov, O. N., Wilks, G. B., Scott, J. M., and Miracle, D. B. (2011). Mechanical properties of Nb$_{25}$Mo$_{25}$Ta$_{25}$W$_{25}$ and V$_{20}$Nb$_{20}$Mo$_{20}$Ta$_{20}$W$_{20}$ refractory high entropy alloys. *Intermetallics* 19, 698–706. doi:10.1016/j.intermet.2011.01.004

Tian, Q., Zhang, G., Yin, K., Wang, W., Cheng, W., and Wang, Y. (2019). The strengthening effects of relatively lightweight AlCoCrFeNi high entropy alloy. *Mater. Char.* 151, 302–309. doi:10.1016/j.matchar.2019.03.006

Tong, C.-J., Chen, Y.-L., Yeh, J.-W., Lin, S.-J., Chen, S.-K., Shun, T.-T., et al. (2005). Microstructure characterization of Al$_x$CoCrCuFeNi high-entropy alloy system with multiprincipal elements. *Metall. Mater. Trans.* 36, 881–893. doi:10.1007/s11661-005-0283-0

Tong, Y., Chen, D., Han, B., Wang, J., Feng, R., Yang, T., et al. (2019). Outstanding tensile properties of a precipitation-strengthened FeCoNiCrTi0.2 high-entropy

alloy at room and cryogenic temperatures. *Acta Mater.* 165, 228–240. doi:10.1016/j.actamat.2018.11.049

Tung, C.-C., Yeh, J.-W., Shun, T.-t., Chen, S.-K., Huang, Y.-S., and Chen, H.-C. (2007). On the elemental effect of AlCoCrCuFeNi high-entropy alloy system. *Mater. Lett.* 61, 1–5. doi:10.1016/j.matlet.2006.03.140

Wang, Z., Huang, Y., Yang, Y., Wang, J., and Liu, C. T. (2015). Atomic-size effect and solid solubility of multicomponent alloys. *Scripta Mater.* 94, 28–31. doi:10.1016/j.scriptamat.2014.09.010

Williamson, G. K., and Hall, W. H. (1953). X-ray line broadening from filed aluminium and wolfram. *Acta Metall.* 1, 22–31. doi:10.1016/0001-6160(53)90006-6

Xiang, S., Luan, H., Wu, J., Yao, K.-F., Li, J., Liu, X., et al. (2019). Microstructures and mechanical properties of CrMnFeCoNi high entropy alloys fabricated using laser metal deposition technique. *J. Alloys Compd.* 773, 387–392. doi:10.1016/j.jallcom.2018.09.235

Yang, T., Xia, S., Liu, S., Wang, C., Liu, S., Zhang, Y., et al. (2015). Effects of AL addition on microstructure and mechanical properties of Al_xCoCrFeNi High-entropy alloy. *Mater. Sci. Eng., A* 648, 15–22. doi:10.1016/j.msea.2015.09.034

Ye, Y. F., Wang, Q., Lu, J., Liu, C. T., and Yang, Y. (2016). High-entropy alloy: challenges and prospects. *Mater. Today.* 19, 349–362. doi:10.1016/j.mattod.2015.11.026

Ye, Y. X., Liu, C. Z., Wang, H., and Nieh, T. G. (2018). Friction and wear behavior of a single-phase equiatomic TiZrHfNb high-entropy alloy studied using a nanoscratch technique. *Acta Mater.* 147, 78–89. doi:10.1016/j.actamat.2018.01.014

Yeh, J.-W. (2013). Alloy Design Strategies and Future Trends in High-Entropy Alloys. *JOM (J. Occup. Med.)* 65, 1759–1771. doi:10.1007/s11837-013-0761-6

Yeh, J.-W., Chen, S.-K., Lin, S.-J., Gan, J.-Y., Chin, T.-S., Shun, T.-T., et al. (2004). Nanostructured high-entropy alloys with multiple principal elements: Novel alloy design concepts and outcomes. *Adv. Eng. Mater.* 6, 299–303. doi:10.1002/adem.200300567 2004

Zhang, B., Liaw, P. K., Brechtl, J., Ren, J., Guo, X., and Zhang, Y. (2020). Effects of Cu and Zn on microstructures and mechanical behavior of the medium-entropy aluminum alloy. *J. Alloys Compd.* 820, 153092. doi:10.1016/j.jallcom.2019.153092

Zhang, H., Pan, Y., and He, Y.-Z. (2011). Synthesis and characterization of FeCoNiCrCu high-entropy alloy coating by laser cladding. *Mater. Des.* 32, 1910–1915. doi:10.1016/j.matdes.2010.12.001

Zhang, Y., Yang, X., and Liaw, P. K. (2012). Alloy Design and Properties Optimization of High-Entropy Alloys. *JOM (J. Occup. Med.)* 64, 830–838. doi:10.1007/s11837-012-0366-5

Zhang, Y., Zhou, Y. J., Lin, J. P., Chen, G. L., and Liaw, P. K. (2008). Solid-Solution Phase Formation Rules for Multi-component Alloys. *Adv. Eng. Mater.* 10, 534–538. doi:10.1002/adem.200700240

Zhang, Y., Zuo, T. T., Tang, Z., Gao, M. C., Dahmen, K. A., Liaw, P. K., et al. (2014). Microstructures and properties of high-entropy alloys. *Prog. Mater. Sci.* 61, 1–93. doi:10.1016/j.pmatsci.2013.10.001

Zhou, Q., Sheikh, S., Ou, P., Chen, D., Hu, Q., and Guo, S. (2019). Corrosion behavior of Hf0.5Nb0.5Ta0.5Ti1.5Zr refractory high-entropy in aqueous chloride solutions. *Electrochem. Commun.* 98, 63–68. doi:10.1016/j.elecom.2018.11.009

Zhuang, Y. X., Liu, W. J., Chen, Z. Y., Xue, H. D., and He, J. C. (2012). Effect of elemental interaction on microstructure and mechanical properties of FeCoNiCuAl alloys. *Mater. Sci. Eng., A* 556, 395–399. doi:10.1016/j.msea.2012.07.003

Zhuang, Y. X., Xue, H. D., Chen, Z. Y., Hu, Z. Y., and He, J. C. (2013). Effect of annealing treatment on microstructures and mechanical properties of FeCoNiCuAl high entropy alloys. *Mater. Sci. Eng., A* 572, 30–35. doi:10.1016/j.msea.2013.01.081

Conflict of Interest: The authors declare that the research was conducted in the absence of any commercial or financial relationships that could be construed as a potential conflict of interest.